Five Degree-of-Freedom Property Interpolation of Arbitrary Grain Boundaries via Voronoi Fundamental Zone Framework

Sterling G. Baird[a,*], Eric R. Homer[a], David T. Fullwood[a], Oliver K. Johnson[a]

[a]*Department of Mechanical Engineering, Brigham Young University, Provo, UT 84602, USA*

Abstract

We apply the Voronoi fundamental zone (VFZ) framework towards gaining insights about the nature of a five degree-of-freedom (5DOF) fundamental zone (FZ) for cubic O_h grain boundaries (GBs). The VFZ framework offers an advantage over other 5DOF based property interpolation methods because it is defined via continuous, Euclidean coordinates and results in rapid distance calculations. Aided by the increased computational efficiency, we find that the maximum dimension of an O_h VFZ is ∼60°, and that nearest neighbor (NN) distances for cubochorically sampled GBs are normally distributed. The VFZ framework allows us to easily identify repeated GBs which in turn enables us to estimate the intrinsic error of the large Fe simulation dataset ($0.065\,\mathrm{J\,m^{-2}}$). We find that the noise and non-uniform sampling make it difficult to resolve low grain boundary energy (GBE) (i.e. cusps) and to validate the model. For the small, low-noise Ni simulation data, we resolve cusps with high accuracy, but uncertainty may be high in regions far from the input data. The trade-offs between noise, dataset size, sampling scheme, and repeat measurements must be carefully managed. Using Gaussian process regression (GPR), we estimate the correlation lengths of the Ni and Fe datasets to be ∼7.4° and 8.3°, respectively, compared with a traditionally accepted value of ∼10°. Finally, we analyze structure-property paths between the Σ3 coherent-twin (CT) GB and other low-Sigma GBs of interest. The methods are based on functions and scripts from (github.com/sgbaird-5dof/interp). Future work involves probing other cubic and non-cubic symmetries and potentially alloys.

Keywords: Grain Boundary, Structure-Property Model, Interpolation, Octonion, Machine Learning

1. Introduction

1.1. Motivation

High fidelity GB structure-property models can accelerate the design and understanding of materials for GB engineering applications such as grain growth (GBE [1], mobility [2], and grain rotation [3–6]), stress-corrosion cracking (diffusivity [7, 8], solubility [9], and segregation [10]) [11–15], strength [16–18], ceramics [19, 20], electronics [21, 22], and thermoelectrics [23]. With the increased use of nanomaterials [16, 22], GBs take on increasingly larger roles as the GB volume fraction becomes significant; this is complicated by the fact that properties of GBs can span orders of magnitude depending on the five macroscopic degrees of freedom (DOFs) [24–26] as well as the three microscopic DOFs [27, 28]. However, the mentioned studies generally only consider a binary classification of GBs or variation of a few DOFs which represents a small "slice" of the full grain boundary character space. Recent advances in high-throughput simulation [26, 29–35], experimental characterization [26, 34, 36–38], and availability of rich GB datasets [33, 35, 39–47] warrant high-fidelity structure-property models capable of

*Corresponding author.

Email address: ster.g.baird@gmail.com (Sterling G. Baird)

handling large amounts of input data to aid in the aforementioned applications.

1.2. Prior Work

Dette et al. [48] builds on the work of Bulatov et al. [49] by predicting the location and number of cusps rather than assuming this a-priori. They provide an equation for uncertainty of predicted values (Equation 7 of [48]) and suggest that their approach is general to alloys and non-cubic crystal systems. While their proposed methods are applicable to 5DOF (as a consequence of being based on Bulatov et al. [49]), they only present results in 1D and 2D subspaces.

Francis et al. [50] derived octonion Spherical Linear Interpolation and provided examples showing that octonion Spherical Linear Interpolation produces smooth, minimum distance paths through GB character space between two arbitrary GBs.

1.3. Voronoi Fundamental Zone Framework

Recently, we introduced a highly efficient method for creating 5DOF structure-property models. We focus on the application of the VFZ framework towards probing and understanding a 5DOF FZ rather than on the computational aspects which have been thoroughly addressed in **?**]. Many of our results depend on functions from `https://github.com/sgbaird-5dof/interp`.

2. Methods

We provide brief summaries of methods related to the VFZ framework (Section 2.1.1).

2.1. The Voronoi Fundamental Zone Framework

The core operations of the VFZ framework are:

1. generating grain boundary octonions (GBOs) (Section 2.1.1)
2. mapping GBOs into a VFZ (Section 2.1.2)
3. calculating distances within the VFZ (Section 2.1.3)

2.1.1. Defining the Voronoi Fundamental Zone

To define a VFZ, an arbitrary, fixed, low-symmetry reference GBO is chosen (o_{ref}) and for our use of GBOs, the VFZ is defined as the region of $\mathbb{S}^7$ (the unit 7-sphere in 8 dimensions) closer to o_{ref} than any of its symmetric images. If a low-symmetry GB is chosen, the point within a VFZ will be unique within numerical tolerance (and hence it is a true FZ). Additionally, we use a Euclidean approximation to the true geodesic distance.

2.1.2. Mapping GBs to the Voronoi Fundamental Zone

A GBO is mapped into a VFZ by calculating the pairwise distances between the reference GBO and each of the symmetrically equivalent octonions and taking the symmetrically equivalent octonion closest to the reference GBO.

2.1.3. Distance Calculations in the Voronoi Fundamental Zone

Once a GBO has been mapped into a VFZ, distance calculations proceed without further consideration of symmetrically equivalent octonions. The VFZ framework suffers from occasional, large distance overestimation which imposes a local sparseness of data and lead to poorer interpolation near the borders of a VFZ. However, this can be mitigated through ensemble or data augmentation techniques.

W

2.1.4. Comparison with Traditional Octonion Framework

The primary differences between the VFZ framework and traditional GBO distance metric are that the VFZ framework is defined by a continuous set of points, exhibits occasional distance overestimation, uses a Euclidean approximation, and has a lower computational complexity.

2.2. Generating Random Voronoi Fundamental Zone Grain Boundary Octonions

We generate random GBOs by a cubochoric approach [51]: we pair two cubochorically sampled GBs to form a GBO.

2.3. Interpolation in the Voronoi Fundamental Zone Framework

While four interpolation methods were tested in the VFZ framework, we focus on GPR which in our case imposes the assumption that crystallographically similar GBs share similar GBEs within some correlation length. GPR has the added benefit of built-in uncertainty quantification.

2.4. Visualizing 5DOF Paths

A modified version of octonion Spherical Linear Interpolation is used to probe a direct path between two GBs in a VFZ. While the direct path in a VFZ is not always the minimum distance path (which may cross the borders of a VFZ), it is instructive to observe these paths as the minimum distance path in 5DOF space is not necessarily the path a GB will take during grain growth.

2.5. Literature Datasets

Ni [42] and Fe [52] GBE datasets from the literature are used. Intrinsic error for the Fe simulation data is estimated by the following steps:

1. Sort GBs into degenerate sets [**?**]
2. Determine the average GBE for each degenerate set
3. Compare each of the degenerate GBs to the set-wise average GBE (root mean square error or mean absolute error)

See Section S5.2 for further details on methods used to estimate intrinsic error of the Fe simulation dataset.

3. Results

We use the VFZ framework to explore properties of a 5DOF FZ. We begin with the following questions:

- What is the intrinsic error of metastable molecular statics (MS) simulations? (Section 3.1)
- When working with randomly generated, symmetrized GBs, how does the number of GBs affect the density and distribution of points? (Section 3.2)
- What are the minimum and maximum dimensions of a 5DOF fundamental zone? (Section 3.3)
- How correlated are nearby GBs w.r.t. crystallography and GBE? (Section 3.4)
- What can crystallographic paths in 5DOF space teach us about material behavior? (Section 3.5)

3.1. Intrinsic Error of Noisy Molecular Statics Simulations

We estimate the intrinsic error of an Fe 0 K MS simulation dataset to be $0.065\,29\,\mathrm{J\,m^{-2}}$ and $0.061\,90\,\mathrm{J\,m^{-2}}$ depending on whether root mean square error or mean absolute error estimates are used, respectively. Minimum and maximum error was $-0.2625\,\mathrm{J\,m^{-2}}$ and $0.2625\,\mathrm{J\,m^{-2}}$, respectively.

3.2. Density and Distribution of Points

Figure 2 illustrates how the Voronoi fundamental zone grain boundary octonion (VFZ-GBO) average NN distance varies with the cardinality of the set (i.e. number of random VFZ-GBOs in the set). The average NN distance (over approximately 70 trials) of set sizes between 388 and 50 000 between $(10.7175 \pm 0.3684)^\circ$ and $(2.6479 \pm 0.2254)^\circ$, respectively. Additionally, a line fit is given. For a specific 50 000 VFZ-GBO set, the NN GBO distance is $(2.870\,90 \pm 0.691\,12)^\circ$ (Figure 1a) while the average 100-th NN distance is within 10° (Figure 1b).

This indicates that, on average, prediction VFZ-GBOs fall within a typically reported GB correlation length[1] of 10° [53] or 15° [42]) of input VFZ-GBOs in large set sizes. We demonstrate that these correlation lengths may be somewhat overestimated (Section 3.4).

[1] Correlation length in the context of GBs has been described as "the degree to which boundaries with the same macroscopic geometrical degrees of freedom in different materials have related properties" [42]

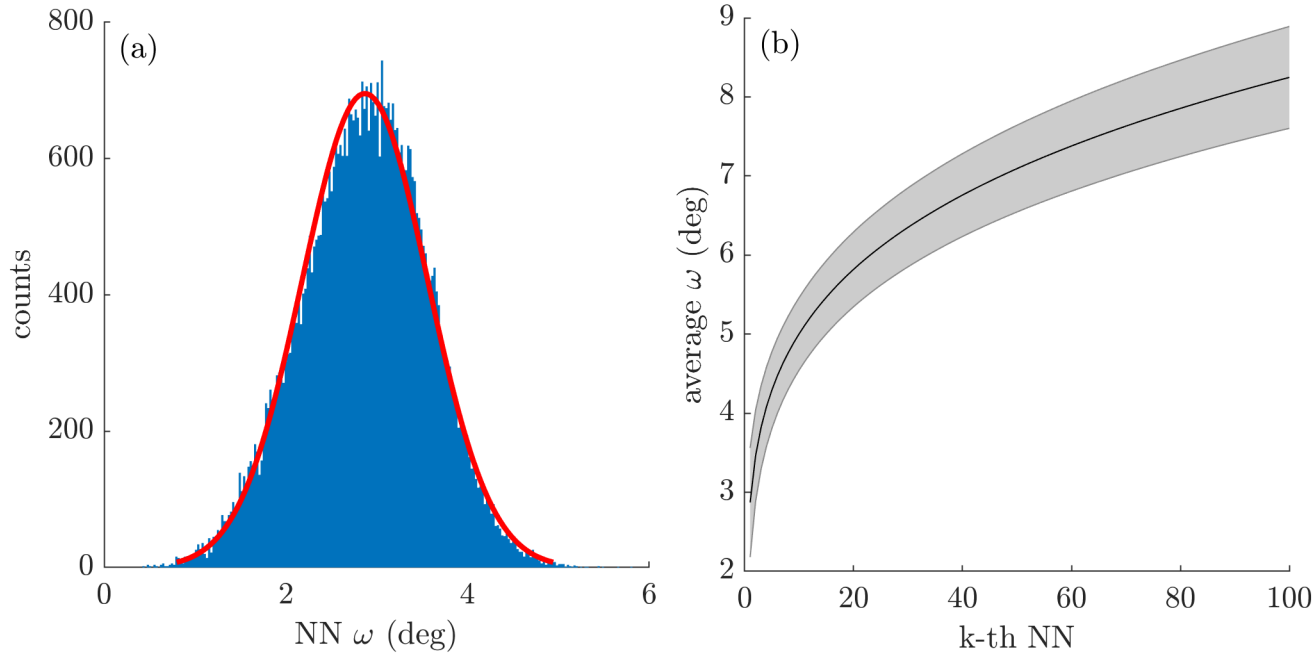

Figure 1: (a) Histogram of NN GBO distances (ω) in a VFZ-GBO set of 50 000 points. The average NN distance was $(2.870\,90 \pm 0.691\,12)^\circ$. (b) The average k-th nearest neighbor distances demonstrate that many nearest neighbors fall within a tight tolerance (less then 10°) out of approximately 10 trial runs.

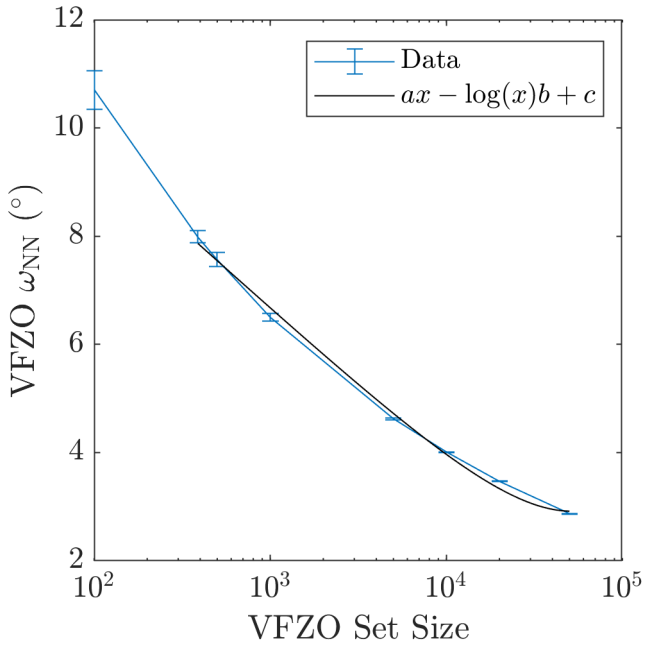

Figure 2: NN VFZ-GBO (ω_{NN}) distances (°) versus VFZ-GBO set size out of 70-80 random VFZ-GBO sets per set size and a fit to $ax - \log(x)b + c$ where $a = 2.5025 \times 10^{-5}$, $b = 1.27396$, $c = 15.4499$, x represents set size, and $388 \leq x \leq 50000$.

3.3. Dimensions of a VFZ

The maximum and minimum dimensions of an O_h cubic VFZ are ∼60° and 99 999°. We also find that the largest minimum (i.e. symmetrized) distance between any two GB is ∼99 999°.

3.4. Correlation Lengths

GPR facilitates analytically solving for correlation lengths, which are determined to be ∼7.4° and 8.3° for the Ni and Fe datasets, respectively. If low noise is assumed for Ni, the correlation length drops to ∼2 degrees. See Table 1 for GPR parameters for each dataset.

By contrast, if a GPR model is trained on a large set of 50 000 GBs sampled from the BRK model, the analytic correlation length is 10.5°.

3.5. 5DOF Paths and GB Behavior

We analyze direct connections between low Sigma GBs of interest to the materials science community. Using the set of 388 GBs defined by Olmsted et al. [42], we choose the Σ5, Σ7, Σ9, and Σ11 GBs with the lowest GBE and visualize direct paths

Table 1: Fitted parameters for two GPR models fitted to the 388 simulated Ni GBEs by Olmsted et al. [43]. The first model allows σ to vary, whereas the second constrains σ to be fixed. σ_L, σ_F, β, and σ are the kernel length scale (°), signal standard deviation (Jm^{-2}), constant basis function (Jm^{-2}), and input property standard deviation (Jm^{-2}), respectively. Also, fitted parameters for a GPR model trained on 80% of the Fe simulation data [NEED TO ADD] and a GPR model trained on 50 000 Bulatov Reed Kumar (BRK) model GBEs are shown [NEED TO ADD].

Fix σ	σ_L (°)	σ_F	β	σ
no	7.3995	0.2049	1.0913	0.0321
yes	1.9354	0.201	1.1044	0.0001

in a VFZ between each of these and the global minimum Σ3 CT GB (Figure 3). This is performed for both the BRK and VFZ-GPR models.

4. Discussion

4.1. Dimensions of a VFZ

What does it mean that the largest dimension is much larger than the smallest dimension? (assuming this is true)

Could correlation lengths be treated separately by rotating a VFZ such that misorientation and boundary plane normals are considered separately?

4.2. Correlation Lengths

The two simulation datasets have distinct differences from each other, as summarized in Table 2.

Table 2: Comparison of Ni (Olmsted et al. [42]) and Fe (Kim et al. [52]) MS simulation datasets. The differences in noise-levels results from whether multiple initial starting configurations were probed in search of a globally minimized configuration as opposed to using a single metastable configuration.

Property	Ni	Fe
Size	388	58604
Noise	Low	High
Symmetry	FCC	BCC

Despite these differences in terms of noise, dataset size, and crystal symmetry, it is interesting to see that the analytic correlation lengths within a VFZ are similar for the two datasets. Both are lower than the correlation lengths of 10° [53] and 15° [42] previously reported[2]. It is reasonable to assume that the Ni data has low noise through use of a global optimization strategy; however, the low correlation length of ∼2° after imposing the low-noise condition suggests that the Ni dataset has an actual correlation length smaller than previously reported. By contrast, the correlation length of a GPR model trained on many BRK GBEs remains relatively large at 10.4°, suggesting that the BRK model is smoothed more than the data warrants on its own. What are the implications? We propose the following:

1. More sophisticated methods are required which do not impose a-priori information about the correlation length[3], but rather let the data itself suggest proper correlation lengths

2. Larger, low-noise datasets which span all 5DOF are needed to be confident in structure-property paths that are not restricted to a single misorientation fundamental zone or boundary plane fundamental zone

We believe that the GPR model within the VFZ framework meets the requirements of point #1 and is capable of handling the more ideal dataset proposed in point #2.

Some questions that remain are:

- Does the similarity between correlation lengths for FCC and BCC extend to non-cubic crystal symmetries?

- What are the differences in correlation length for other properties? (e.g. mobility)

It is possible that the correlation length may increase with the size of the VFZs, and we expect that

[2]Both of these lengths are based on results from Olmsted et al. [42]

[3]The a-priori information that the BRK model imposes is that correlation lengths within a misorientation fundamental zone or boundary plane fundamental zone hold for arbitrary paths through 5DOF space.

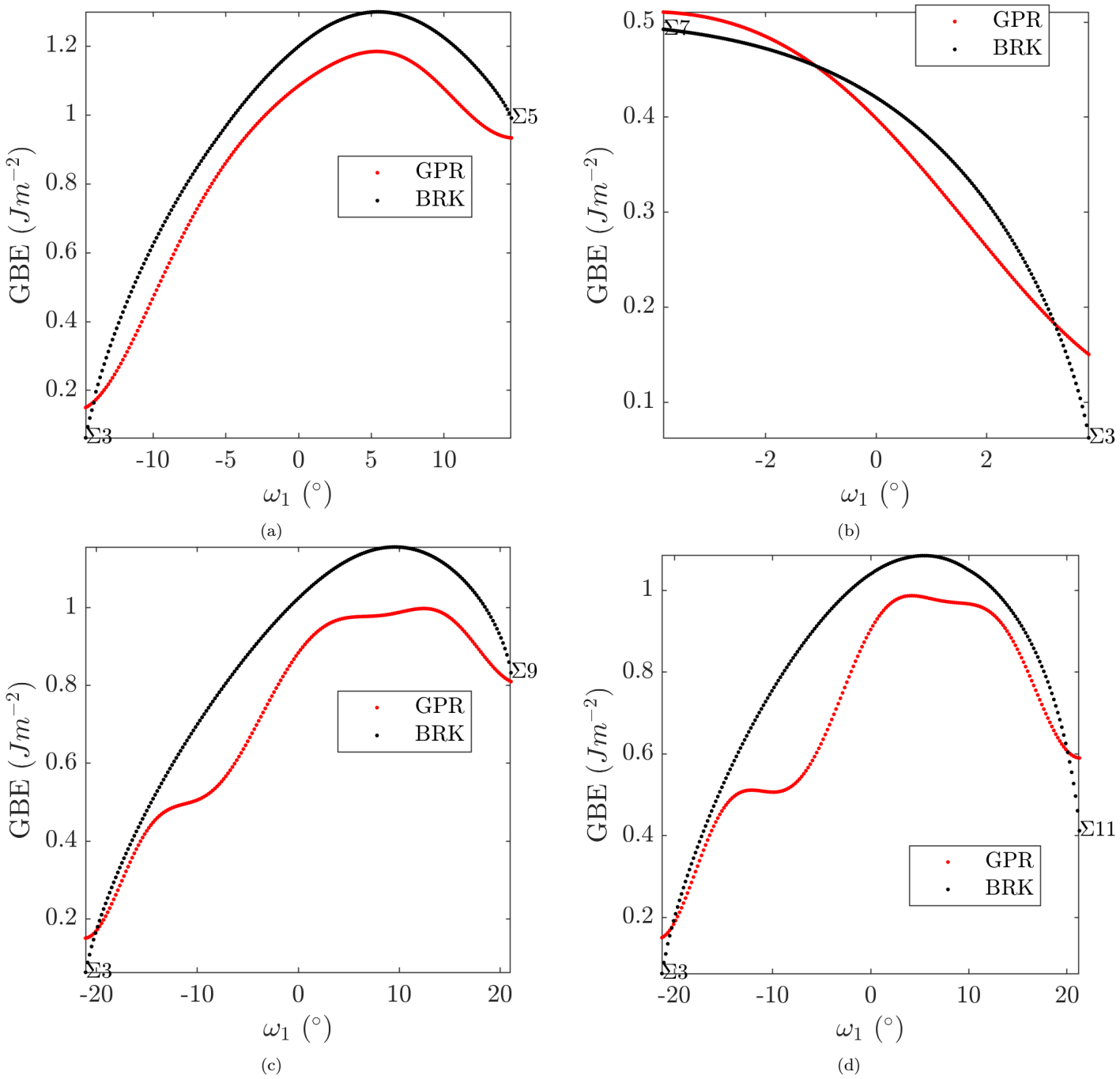

Figure 3: GBEs along direct paths in a VFZ between the Σ3 CT boundary and minimum GBE (a) Σ5, (b) Σ7, (c) Σ9, and (d) Σ11 GBs within the Olmsted et al. [42] dataset. GBE values are plotted for the BRK and GPR models which both used Olmsted et al. [42] as input data.

the correlation length will depend on the property of interest.

4.3. 5DOF Paths

We observe that Σ3 and Σ7 are connected (i.e. no activation energy barrier) while the direct paths between Σ3 and Σ5, Σ9, Σ11 are separated by energy barriers. This indicates that for grain growth systems governed by GBE, Σ7 GBs will spontaneously transform into Σ3 CT GBs, whereas if Σ5, Σ9, Σ11 transform into Σ3 CTs, this will need to occur either by overcoming the activation energy or via paths through 5DOF space other than the ones shown.

4.4. Potential for Numerical Derivatives

Additionally, these visualizations suggest the ability to estimate numerical derivatives or gradients of GB properties without being restricted to a GB subspace (e.g. misorientation fundamental zone or boundary plane fundamental zone) which can be a useful mathematical construct for the GB community. For example, steepest descent paths and all local GBE minima can be estimated and used in grain growth simulations. In such contexts, use of ensembled VFZ-GBO interpolation or data augmentation may be necessary to mitigate discontinuity artifacts when crossing the exterior of a VFZ as discussed in Section 2.1.3. We plan to explore this in future work.

4.5. Literature Datasets

We analyze implications of results for a Gaussian process regression mixture model developed for a noisy, Fe MS simulation dataset. We find that:

- the model error is on par with the intrinsic error of the data

4.5.1. Overprediction Bias

Next, given the theoretical existence of a true minimum GBE for a given GB, the predictions which were based on metastable GBEs can be assumed to have an overprediction bias relative to the true minimum. On average, we expect this overprediction bias relative to the true minimum GBE (rather than the most likely metastable state) may be on the order of a few hundred $\mathrm{mJ\,m^{-2}}$ and may vary as a function of true minimum GBE. In other words, the model obtained is probably an estimate of the most likely metastable GBE rather than the true minimum GBE. This is akin to saying that we obtain from this data a model that approximates the non-equilibrium, Stillinger quenched red curve of Figure 4(c1) in [27], not the minimum GBE blue curve of the same chart. See [27] for an in-depth treatment of equilibrium and metastable GBE.

4.5.2. Improving on Existing Datasets

Finally, datasets where multiple metastable GBEs (e.g. 3-10 repeats) are provided for each GB will likely greatly improve the performance of the GPR model in predicting either the most likely metastable GBE (when all GBEs are considered) or the true minimum GBE (when only the minimum GBE is considered for each GB) and may even negate the need for a Gaussian process regression mixture approach. Thus, it is suggested that, where feasible, future large-scale GB bicrystal simulation studies report all property data for repeated trial runs rather than a single trial run or a single value from a set of trial runs. Ideally, data for the three additional microscopic DOFs for GBs (which falls into the category of epistemic uncertainty in this work) would also be included. We believe it is likely that minimum energy paths (i.e. paths of steepest descent) in the GBE landscape depend on both macroscopic and microscopic DOFs (in total, 8DOF) and could offer a more holistic view of GB behavior that better mimics and explains experimental grain growth observations. Indeed, it has been experimentally observed that at least some GB migration mechanisms involve structural transformations between equilibrium GBs via metastable states [28].

5. Conclusion

We applied the VFZ framework to learning more about the nature of a 5DOF FZ. The increase of distance computation throughput and the development of a 5DOF VFZ with continuous coordinates enabled us to explore the nature of a 5DOF FZ. We found that symmetrized NN distances are Gaussian and plotted these as a function of set size. We determined the maximum and minimum dimensions of an O_h VFZ to be $\sim$60° and 99 999°, respectively.

Other point groups (in particular those which are noncentrosymmetric) may give rise to differently shaped/larger VFZs and for which

the Euclidean approximation may need to be dropped. It will be interesting to see the VFZ framework applied for other distance metrics (see Morawiec [54] for a comprehensive summary of metrics). The GPR interpolation errors (50 000 VFZ-GBOs) for the BRK validation model are about 2.4 times the intrinsic error that would be expected from reconstruction of noise-free, experimental polycrystalline data via locally optimal block preconditioned conjugate gradient [55] (180 000 GBs) with their simpler validation model. Moreover, the interpolation errors for a Fe simulation dataset are on par with the intrinsic errors of the dataset itself (Section S5.2). Analysis of the GPR fitting results indicates that the Ni and Fe simulation datasets have correlation lengths of 8.3° and 7.4°, respectively. We recommend the GPR interpolation method for the VFZ framework for most applications because it provides the best combination of accuracy and speed, handles input noise, and has built-in uncertainty quantification; however, the other methods can meet niche needs. For example, barycentric interpolation enables rapid and accurate predictions when the function to be evaluated changes, but the input and prediction GBs remain fixed.

We anticipate that in addition to GB property interpolation, the VFZ framework will continue to reveal important aspects of a 5DOF FZ and inform us about material behavior especially w.r.t. grain growth and other large scale time-dependent or iterative processes.

Acknowledgement

The authors thank Ian Chesser, Toby Francis, Victoria Baird, Brandon Snow, and José Niño for useful discussions. This work was supported by the National Science Foundation under Grant No. 1610077. This work was supported in part through computational resources provided by Brigham Young University's Office of Research Computing.

CRediT Statement

Sterling Baird: Conceptualization, Methodology, Software, Validation, Formal analysis, Investigation, Data Curation, Writing - Original Draft, Writing - Review & Editing, Visualization. **Oliver Johnson**: Supervision, Project administration, Funding acquisition, Conceptualization, Writing - Review & Editing. **David Fullwood**: Funding acquisition, Writing - Review & Editing. **Eric Homer**: Funding acquisition, Writing - Review & Editing

Appendix A Active vs. Passive Convention

Misorientation quaternions are represented in the active sense[4]:

$$q_m = {q_A}^{-1} q_B \tag{1}$$

where q_m, q_A, and q_B represent the misorientation quaternion, orientation quaternion of grain A in the sample frame, and orientation quaternion of grain B in the sample frame, respectively. The $^{-1}$ operator denotes a unit quaternion inverse (identical to conjugation of a unit quaternion). Quaternion multiplication is given by equation 23 of [56]

$$pq \equiv (p_0 q_0 - \mathbf{p} \cdot \mathbf{q}, q_0 \mathbf{p} + p_0 \mathbf{q} + P \mathbf{p} \times \mathbf{q}) \tag{2}$$

where q_0 and p_0 are scalar components of the quaternions, and $\mathbf{q}$ and $\mathbf{p}$ are the vector components.

In this work, we use the convention that $P = 1$ throughout the various operations in the VFZ repository ($P \equiv$ `epsijk`) and highly encourage interested readers to refer to Rowenhorst et al. [56] to understand the redefined versions of quaternion multiplication, quaternion rotation, nuances associated with use of active vs. passive conventions, etc. Boundary plane

[4] The passive convention is used in [50]

unit normals are expressed pointing away from grain A and in the reference frame of grain A (i.e. the outward-pointing normal convention).

Glossary

5DOF five degree-of-freedom 1–3, 5–8

BRK Bulatov Reed Kumar 4–6, 8

CT coherent-twin 1, 5, 6

DOF degree of freedom 1, 7

FZ fundamental zone 1–3, 7, 8

GB grain boundary 1–8

GBE grain boundary energy 1, 3–7

GBO grain boundary octonion 2–4

GPR Gaussian process regression 1, 3–8

MS molecular statics 3, 5, 7

NN nearest neighbor 1, 3, 4, 7

VFZ Voronoi fundamental zone 1–8

VFZ-GBO Voronoi fundamental zone grain boundary octonion 3, 4, 7, 8

References

[1] S. Jin, M. Huang, Y. Kwon, L. Zhang, B. W. Li, S. Oh, J. Dong, D. Luo, M. Biswal, B. V. Cunning, P. V. Bakharev, I. Moon, W. J. Yoo, D. C. Camacho-Mojica, Y. J. Kim, S. H. Lee, B. Wang, W. K. Seong, M. Saxena, F. Ding, H. J. Shin, R. S. Ruoff, Colossal grain growth yields single-crystal metal foils by contact-free annealing, Science 362 (2018) 1021–1025. doi:10.1126/science.aao3373.

[2] J. E. Brandenburg, L. A. Barrales-Mora, D. A. Molodov, On migration and faceting of low-angle grain boundaries: Experimental and computational study, Acta Materialia 77 (2014) 294–309. doi:10.1016/j.actamat.2014.06.006.

[3] Z. Huang, M. Bartels, R. Xu, M. Osterhoff, S. Kalbfleisch, M. Sprung, A. Suzuki, Y. Takahashi, T. N. Blanton, T. Salditt, J. Miao, Grain rotation and lattice deformation during photoinduced chemical reactions revealed by in situ X-ray nanodiffraction, Nature Materials 14 (2015) 691–695. doi:10.1038/nmat4311.

[4] Z. Trautt, Y. Mishin, Capillary-driven grain boundary motion and grain rotation in a tricrystal: A molecular dynamics study, Acta Materialia 65 (2014) 19–31. doi:10.1016/j.actamat.2013.11.059.

[5] H. Sharma, R. M. Huizenga, A. Bytchkov, J. Sietsma, S. E. Offerman, Observation of changing crystal orientations during grain coarsening, Acta Materialia 60 (2012) 229–237. doi:10.1016/j.actamat.2011.09.057.

[6] L. G. Ware, D. H. Suzuki, K. R. Wicker, Z. C. Cordero, Grain boundary plane manipulation in directionally solidified bicrystals and tricrystals, Scripta Materialia 152 (2018) 98–101. doi:10.1016/j.scriptamat.2018.03.047.

[7] J. Li, A. Oudriss, A. Metsue, J. Bouhattate, X. Feaugas, Anisotropy of hydrogen diffusion in nickel single crystals: The effects of self-stress and hydrogen concentration on diffusion, Scientific Reports 7 (2017) 45041. doi:10.1038/srep45041.

[8] A. Oudriss, J. Creus, J. Bouhattate, E. Conforto, C. Berziou, C. Savall, X. Feaugas, Grain size and grain-boundary effects on diffusion and trapping of hydrogen in pure nickel, Acta Materialia 60 (2012) 6814–6828. doi:10.1016/j.actamat.2012.09.004.

[9] A. Metsue, A. Oudriss, X. Feaugas, Hydrogen solubility and vacancy concentration in nickel single crystals at thermal equilibrium: New insights from statistical mechanics and ab initio calculations,

Journal of Alloys and Compounds 656 (2016) 555–567. doi:10.1016/j.jallcom.2015.09.252.

[10] S. Huang, D. Chen, J. Song, D. L. McDowell, T. Zhu, Hydrogen embrittlement of grain boundaries in nickel: An atomistic study, npj Computational Materials 3 (2017) 1–8. doi:10.1038/s41524-017-0031-1.

[11] S. Xia, H. Li, T. G. Liu, B. X. Zhou, Appling grain boundary engineering to Alloy 690 tube for enhancing intergranular corrosion resistance, Journal of Nuclear Materials 416 (2011) 303–310. doi:10.1016/j.jnucmat.2011.06.017.

[12] M. J. Demkowicz, A threshold density of helium bubbles induces a ductile-to-brittle transition at a grain boundary in nickel, Journal of Nuclear Materials 533 (2020) 152118. doi:10.1016/j.jnucmat.2020.152118.

[13] J. P. Hanson, A. Bagri, J. Lind, P. Kenesei, R. M. Suter, S. Gradečak, M. J. Demkowicz, Crystallographic character of grain boundaries resistant to hydrogen-assisted fracture in Ni-base alloy 725, Nature Communications 9 (2018) 1–11. doi:10.1038/s41467-018-05549-y.

[14] S. Jothi, S. V. Merzlikin, T. N. Croft, J. Andersson, S. G. Brown, An investigation of micro-mechanisms in hydrogen induced cracking in nickel-based superalloy 718, Journal of Alloys and Compounds 664 (2016) 664–681. doi:10.1016/j.jallcom.2016.01.033.

[15] X. Zhou, D. Marchand, D. L. McDowell, T. Zhu, J. Song, Chemomechanical Origin of Hydrogen Trapping at Grain Boundaries in fcc Metals, Physical Review Letters 116 (2016) 1–33. doi:10.1103/PhysRevLett.116.075502.

[16] W. Huang, M. Shishehbor, N. Guarín-Zapata, N. D. Kirchhofer, J. Li, L. Cruz, T. Wang, S. Bhowmick, D. Stauffer, P. Manimunda, K. N. Bozhilov, R. Caldwell, P. Zavattieri, D. Kisailus, A natural impact-resistant bicontinuous composite nanoparticle coating, Nature Materials 19 (2020) 1236–1243. doi:10.1038/s41563-020-0768-7.

[17] Y. M. Wang, T. Voisin, J. T. McKeown, J. Ye, N. P. Calta, Z. Li, Z. Zeng, Y. Zhang, W. Chen, T. T. Roehling, R. T. Ott, M. K. Santala, P. J. Depond, M. J. Matthews, A. V. Hamza, T. Zhu, Additively manufactured hierarchical stainless steels with high strength and ductility, Nature Materials 17 (2018) 63–71. doi:10.1038/nmat5021.

[18] N. Y. C. Lin, M. Bierbaum, P. Schall, J. P. Sethna, I. Cohen, Measuring nonlinear stresses generated by defects in 3D colloidal crystals, Nature Materials 15 (2016) 1172–1176. doi:10.1038/nmat4715.

[19] D. Yin, C. Chen, M. Saito, K. Inoue, Y. Ikuhara, Ceramic phases with one-dimensional long-range order, Nature Materials 18 (2019) 19–23. doi:10.1038/s41563-018-0240-0.

[20] Y. Guan, W. Li, Y. Gong, G. Liu, X. Zhang, J. Chen, J. Gelb, W. Yun, Y. Xiong, Y. Tian, H. Wang, Analysis of the three-dimensional microstructure of a solid-oxide fuel cell anode using nano X-ray tomography, Journal of Power Sources 196 (2011) 1915–1919. doi:10.1016/j.jpowsour.2010.09.059.

[21] I. V. Vlassiouk, Y. Stehle, P. R. Pudasaini, R. R. Unocic, P. D. Rack, A. P. Baddorf, I. N. Ivanov, N. V. Lavrik, F. List, N. Gupta, K. V. Bets, B. I. Yakobson, S. N. Smirnov, Evolutionary selection growth of two-dimensional materials

on polycrystalline substrates, Nature Materials 17 (2018) 318–322. doi:10.1038/s41563-018-0019-3.

[22] Y. Han, M.-Y. Li, G.-S. Jung, M. A. Marsalis, Z. Qin, M. J. Buehler, L.-J. Li, D. A. Muller, Sub-nanometre channels embedded in two-dimensional materials, Nature Materials 17 (2018) 129–133. doi:10.1038/nmat5038.

[23] J. Sun, J. Yu, Y. Guo, Q. Wang, Enhancing power factor of SnSe sheet with grain boundary by doping germanium or silicon, npj Computational Materials 6 (2020) 1–6. doi:10.1038/s41524-020-00368-6.

[24] O. K. Johnson, L. Li, M. J. Demkowicz, C. A. Schuh, Inferring grain boundary structure–property relations from effective property measurements, Journal of Materials Science 50 (2015) 6907–6919. doi:10.1007/s10853-015-9241-4.

[25] C.-C. Yang, A. Rollett, W. Mullins, Measuring relative grain boundary energies and mobilities in an aluminum foil from triple junction geometry, Scripta Materialia 44 (2001) 2735–2740. doi:10.1016/S1359-6462(01)00960-5.

[26] J. Zhang, W. Ludwig, Y. Zhang, H. H. B. Sørensen, D. J. Rowenhorst, A. Yamanaka, P. W. Voorhees, H. F. Poulsen, Grain boundary mobilities in polycrystals, Acta Materialia 191 (2020) 211–220. doi:10.1016/j.actamat.2020.03.044.

[27] J. Han, V. Vitek, D. J. Srolovitz, Grain-boundary metastability and its statistical properties, Acta Materialia 104 (2016) 259–273. doi:10.1016/j.actamat.2015.11.035.

[28] J. Wei, B. Feng, R. Ishikawa, T. Yokoi, K. Matsunaga, N. Shibata, Y. Ikuhara, Direct imaging of atomistic grain boundary migration, Nature Materials (2021). doi:10.1038/s41563-020-00879-z.

[29] R. Bostanabad, A. T. Bui, W. Xie, D. W. Apley, W. Chen, Stochastic microstructure characterization and reconstruction via supervised learning, Acta Materialia 103 (2016). doi:10.1016/j.actamat.2015.09.044.

[30] E. R. Homer, High-throughput simulations for insight into grain boundary structure-property relationships and other complex microstructural phenomena, Computational Materials Science 161 (2019) 244–254. doi:10.1016/j.commatsci.2019.01.041.

[31] S. Jothi, T. N. Croft, S. G. Brown, Multiscale multiphysics model for hydrogen embrittlement in polycrystalline nickel, Journal of Alloys and Compounds 645 (2015) S500–S504. doi:10.1016/j.jallcom.2014.12.073.

[32] H. Pirgazi, On the alignment of 3D EBSD data collected by serial sectioning technique, Materials Characterization 152 (2019) 223–229. doi:10.1016/j.matchar.2019.04.026.

[33] H. Pirgazi, K. Glowinski, A. Morawiec, L. A. Kestens, Three-dimensional characterization of grain boundaries in pure nickel by serial sectioning via mechanical polishing, Journal of Applied Crystallography 48 (2015) 1672–1678. doi:10.1107/S1600576715017616.

[34] A. Speidel, R. Su, J. Mitchell-Smith, P. Dryburgh, I. Bisterov, D. Pieris, W. Li, R. Patel, M. Clark, A. T. Clare, Crystallographic texture can be rapidly determined by electrochemical surface analytics, Acta Materialia 159 (2018) 89–101. doi:10.1016/J.ACTAMAT.2018.07.059.

[35] H. Zheng, X. G. Li, R. Tran, C. Chen, M. Horton, D. Winston, K. A. Persson, S. P. Ong, Grain boundary properties of elemental metals, Acta Materialia 186

(2020) 40–49. doi:10.1016/j.actamat.2019.12.030. arXiv:1907.08905.

[36] R. Keinan, H. Bale, N. Gueninchault, E. Lauridsen, A. Shahani, Integrated imaging in three dimensions: Providing a new lens on grain boundaries, particles, and their correlations in polycrystalline silicon, Acta Materialia 148 (2018) 225–234. doi:10.1016/J.ACTAMAT.2018.01.045.

[37] M. Seita, M. Volpi, S. Patala, I. McCue, C. A. Schuh, M. V. Diamanti, J. Erlebacher, M. J. Demkowicz, A high-throughput technique for determining grain boundary character nondestructively in microstructures with through-thickness grains, Npj Computational Materials 2 (2016) 16016. URL: http://dx.doi.org/10.1038/npjcompumats.2016.16.

[38] B. Winiarski, A. Gholinia, K. Mingard, M. Gee, G. Thompson, P. Withers, Broad ion beam serial section tomography, Ultramicroscopy 172 (2017) 52–64. doi:10.1016/j.ultramic.2016.10.014.

[39] H. K. Kim, W. S. Ko, H. J. Lee, S. G. Kim, B. J. Lee, An identification scheme of grain boundaries and construction of a grain boundary energy database, Scripta Materialia 64 (2011) 1152–1155. doi:10.1016/j.scriptamat.2011.03.020.

[40] S. Li, L. Yang, C. Lai, Atomistic simulations of energies for arbitrary grain boundaries. Part I: Model and validation, Computational Materials Science 161 (2019) 330–338. doi:10.1016/j.commatsci.2019.02.003.

[41] J. Li, S. J. Dillon, G. S. Rohrer, Relative grain boundary area and energy distributions in nickel, Acta Materialia 57 (2009) 4304–4311. doi:10.1016/j.actamat.2009.06.004.

[42] D. L. Olmsted, E. A. Holm, S. M. Foiles, Survey of computed grain boundary properties in face-centered cubic metals-II: Grain boundary mobility, Acta Materialia 57 (2009) 3704–3713. doi:10.1016/j.actamat.2009.04.015.

[43] D. L. Olmsted, S. M. Foiles, E. A. Holm, Survey of computed grain boundary properties in face-centered cubic metals: I. Grain boundary energy, Acta Materialia 57 (2009) 3694–3703. doi:10.1016/j.actamat.2009.04.007.

[44] V. Randle, G. S. Rohrer, H. M. Miller, M. Coleman, G. T. Owen, Five-parameter grain boundary distribution of commercially grain boundary engineered nickel and copper, Acta Materialia 56 (2008) 2363–2373. doi:10.1016/j.actamat.2008.01.039.

[45] D. M. Saylor, A. Morawiec, B. L. Adams, G. S. Rohrer, Misorientation dependence of the grain boundary energy in magnesia, Interface Science 8 (2000) 131–140. doi:10.1023/A:1008764219575.

[46] D. M. Saylor, A. Morawiec, G. S. Rohrer, The relative free energies of grain boundaries in magnesia as a function of five macroscopic parameters, Acta Materialia 51 (2003) 3675–3686. doi:10.1016/S1359-6454(03)00182-4.

[47] L. Yang, C. Lai, S. Li, Atomistic simulations of energies for arbitrary grain boundaries. Part II: Statistical analysis of energies for tilt and twist grain boundaries, Computational Materials Science 162 (2019) 268–276. doi:10.1016/j.commatsci.2019.03.010.

[48] H. Dette, J. Gösmann, C. Greiff, R. Janisch, Efficient sampling in materials simulation - Exploring the parameter space of grain boundaries, Acta Materialia 125 (2017) 145–155. doi:10.1016/j.actamat.2016.11.044.

[49] V. V. Bulatov, B. W. Reed, M. Kumar, Grain boundary energy function for fcc metals, Acta Materialia 65 (2014) 161–175. doi:10.1016/j.actamat.2013.10.057.

[50] T. Francis, I. Chesser, S. Singh, E. A. Holm, M. De Graef, A geodesic octonion metric for grain boundaries, Acta Materialia 166 (2019) 135–147. doi:10.1016/j.actamat.2018.12.034.

[51] S. Singh, M. De Graef, Orientation sampling for dictionary-based diffraction pattern indexing methods, Modelling and Simulation in Materials Science and Engineering 24 (2016). doi:10.1088/0965-0393/24/8/085013.

[52] H.-K. Kim, S. G. Kim, W. Dong, I. Steinbach, B.-J. Lee, Phase-field modeling for 3D grain growth based on a grain boundary energy database, Modelling and Simulation in Materials Science and Engineering 22 (2014) 034004. doi:10.1088/0965-0393/22/3/034004.

[53] G. S. Rohrer, E. A. Holm, A. D. Rollett, S. M. Foiles, J. Li, D. L. Olmsted, Comparing calculated and measured grain boundary energies in nickel, Acta Materialia 58 (2010) 5063–5069. doi:10.1016/j.actamat.2010.05.042.

[54] A. Morawiec, On distances between grain interfaces in macroscopic parameter space, Acta Materialia 181 (2019) 399–407. doi:10.1016/j.actamat.2019.09.032.

[55] Y. F. Shen, X. Zhong, H. Liu, R. M. Suter, A. Morawiec, G. S. Rohrer, Determining grain boundary energies from triple junction geometries without discretizing the five-parameter space, Acta Materialia 166 (2019) 126–134. doi:10.1016/j.actamat.2018.12.022.

[56] D. Rowenhorst, A. D. Rollett, G. S. Rohrer, M. Groeber, M. Jackson, P. J. Konijnenberg, M. De Graef, Consistent representations of and conversions between 3D rotations, Modelling and Simulation in Materials Science and Engineering 23 (2015) 083501. doi:10.1088/0965-0393/23/8/083501.